

Simultaneous Resonant and Broadband Detection for Dark Sectors

Yifan Chen,¹ Chunlong Li,² Yuxin Liu,^{3,4} Jing Shu,^{5,6,7} Yuting Yang,^{2,4} and Yanjie Zeng^{2,4}

¹*Niels Bohr International Academy, Niels Bohr Institute, Blegdamsvej 17, 2100 Copenhagen, Denmark*

²*CAS Key Laboratory of Theoretical Physics, Institute of Theoretical Physics, Chinese Academy of Sciences, Beijing 100190, China*

³*International Center for Theoretical Physics Asia-Pacific, Beijing/Hangzhou, China*

⁴*School of Physical Sciences, University of Chinese Academy of Sciences, Beijing 100049, China*

⁵*School of Physics and State Key Laboratory of Nuclear Physics and Technology, Peking University, Beijing 100871, China*

⁶*Center for High Energy Physics, Peking University, Beijing 100871, China*

⁷*Beijing Laser Acceleration Innovation Center, Huairou, Beijing, 101400, China*

(Dated: September 25, 2023)

Electromagnetic resonant systems, such as cavities or LC circuits, have emerged as powerful detectors for probing ultralight boson dark matter and high-frequency gravitational waves. However, the limited resonant bandwidth of conventional single-mode resonators, imposed by quantum fluctuations, necessitates numerous scan steps to cover broad unexplored frequency regions. The incorporation of multiple auxiliary modes can realize a broadband detector while maintaining a substantial signal response. The broadened sensitive width can be on the same order as the resonant frequency, encompassing several orders of the source frequency for heterodyne detection, where a background cavity mode transitions into another. Consequently, our approach enables significantly deeper exploration of the parameter space within the same integration time compared to single-mode detection.

Introduction — Axions [1–3] and dark photons [4] are compelling candidates for dark matter (DM) due to their natural prediction in the compactification of higher dimensional fundamental theories [5–8]. The QCD axion, in particular, provides a solution to the strong CP problem [9]. Experimental efforts are underway to detect these bosonic DM candidates through their electromagnetic coupling, using techniques like resonant microwave cavities [10, 11] and superconducting circuits [12–14]. In both cases, axions in the presence of a strong background magnetic field or dark photons can induce effective currents, which serve as signals in the haloscope experiments [15–21].

On the other hand, gravitational waves (GW) with frequencies higher than kHz can offer insights into particle physics beyond the standard model and early universe cosmology [22]. Two noteworthy phenomena, namely, the inverse Gertsenshtein effect [23] akin to axion electrodynamics, and mechanical resonance [24–26], have the capability to convert GW into photons in the presence of a background electromagnetic field. The the largely unexplored parameter space of high frequency GW has gained significant attention, leading to the implementation of axion haloscope experiments aimed at detecting its signatures [27–33].

The scan rate is a crucial figure of merit for covering a broad frequency range [34–37], influenced by the trade-off between the bandwidth of each scan and its signal response for resonant detection. In a single-mode resonator, the response to the signal becomes indistinguishable from intrinsic fluctuations, making the effective bandwidth of each scan the range where intrinsic noise dominates over the readout noise [38, 39]. Hence, optimizing the readout coupling allows for achieving a

saturated standard quantum limit [34, 35, 37–43].

Exceeding the standard quantum limit of single-mode resonators involves further broadening the effective bandwidth. One practical approach to achieve this is by reducing readout noise through squeezing [34–37]. Recently, several studies have demonstrated that a multi-mode resonant system with auxiliary non-degenerate parametric interactions can significantly increase the response to signals in the off-resonant frequency region, leading to a considerably broader effective bandwidth [44–46].

In this study, we establish the quantum limit of the scan rate for multi-mode resonant systems. This newly derived limit allows experiments to achieve a bandwidth as large as the resonant frequency for each scan. More notably, by applying the multi-mode generalization to heterodyne upconversion detections, where the bosonic fields induce transitions between two quasi-degenerate modes [32, 41, 42, 47], it becomes feasible to realize a simultaneous resonant and broadband detector. This means achieving a significant response to signals while obtaining an effective bandwidth that spans several orders in the frequency domain.

Quantum limit for single-mode resonators — The interaction Hamiltonian describing the coupling between a cavity or a circuit mode (\hat{a}) and the background bosonic field (Ψ) in the interaction picture is given by:

$$H_\alpha = \alpha\Psi (\hat{a} e^{i\omega_{\text{rf}}t} + \hat{a}^\dagger e^{-i\omega_{\text{rf}}t}) / \sqrt{2}. \quad (1)$$

Here, α represents the coupling constant, and ω_{rf} is the resonant frequency of \hat{a} . Apart from the signal mode, fluctuations are induced by intrinsic dissipation and readout systems. These contributions can be expressed in the

frequency domain using power spectral densities (PSDs):

$$\begin{aligned} S_{\text{sig}} &= |S_{0r}|^2 \frac{\alpha^2}{4\gamma} S_{\Psi}, \\ S_{\text{noise}} &= |S_{0r}|^2 n_{\text{occ}} + |S_{rr}|^2 \frac{1}{2} + \frac{1}{2}. \end{aligned} \quad (2)$$

Here, n_{occ} represents the noise occupation number. Specifically, for thermal noise, its value is given by $1/2 + 1/(e^{\omega/T} - 1)$, where ω represents the frequency and T denotes the temperature. The parameter $\gamma \equiv \omega/(2Q_{\text{int}})$ corresponds to the intrinsic dissipation coefficient, and S_{Ψ} is the PSD of bosonic sources. The two scattering matrix elements, characterizing the propagation from the input to the output of different ports, are given by:

$$S_{0r} = -\frac{2\sqrt{\gamma\gamma_r}}{\gamma + \gamma_r - i\Omega}, \quad S_{rr} = \frac{\gamma - \gamma_r - i\Omega}{\gamma + \gamma_r - i\Omega}. \quad (3)$$

Here, the subscript 0 represents the probing sensor, and r indicates the readout port. γ_r represents the tunable coupling of the readout, and $\Omega \equiv \omega - \omega_{\text{rf}}$ is the frequency shift from ω_{rf} . Eq. 2 includes intrinsic fluctuation noise and readout noise with an additional 1/2 from amplifiers, respectively. In the zero-temperature limit, their sum is precisely one due to unitarity, leading to the standard quantum limit of single-mode resonant detection [38, 39].

The sensitivity reach of each scan can be estimated by imposing a requirement that the signal-to-noise ratio (SNR) be of order one [38, 39, 41–43, 45], as described by the Dicke radiometer equation [48]:

$$\text{SNR}^2 = \frac{t_{\text{int}}}{2\pi} \int_0^{\infty} \left(\frac{S_{\text{sig}}}{S_{\text{noise}}} \right)^2 d\omega. \quad (4)$$

Here, t_{int} is the integration time. The integrand in Eq. (4) is a product of two distributions: $\alpha^4 S_{\Psi}^2/\gamma^2$ and the sensitive response function of the detector, characterized by $(|S_{0r}|^2 n_{\text{occ}}/S_{\text{noise}})^2$. For simplicity, we parameterize the sources using an average frequency $\bar{\omega}_{\Psi}$ and a bandwidth $\Delta\omega_{\Psi}$, where $\Delta\omega_{\Psi}/\bar{\omega}_{\Psi}$ is 10^{-6} for non-relativistic DM. On the other hand, due to the common factor $|S_{0r}|^4$ of the signal and intrinsic fluctuation in Eq. (4), the width of the sensitive response function is approximately

$$\Delta\omega_r \equiv \int_0^{\infty} \left(\frac{|S_{0r}|^2 n_{\text{occ}}}{S_{\text{noise}}} \right)^2 d\omega. \quad (5)$$

This quantity quantifies the range where intrinsic noise dominates the rest. The integral width in Eq. (4) is determined by the minimum of $\Delta\omega_{\Psi}$ and $\Delta\omega_r$. Moreover, their maximum controls how the integration time t_{int} of each scan is distributed within the total amount of time t_e spent covering each e -fold of $\bar{\omega}_{\Psi}$:

$$t_{\text{int}} \simeq t_e \max[\Delta\omega_{\Psi}, \Delta\omega_r] / \bar{\omega}_{\Psi}. \quad (6)$$

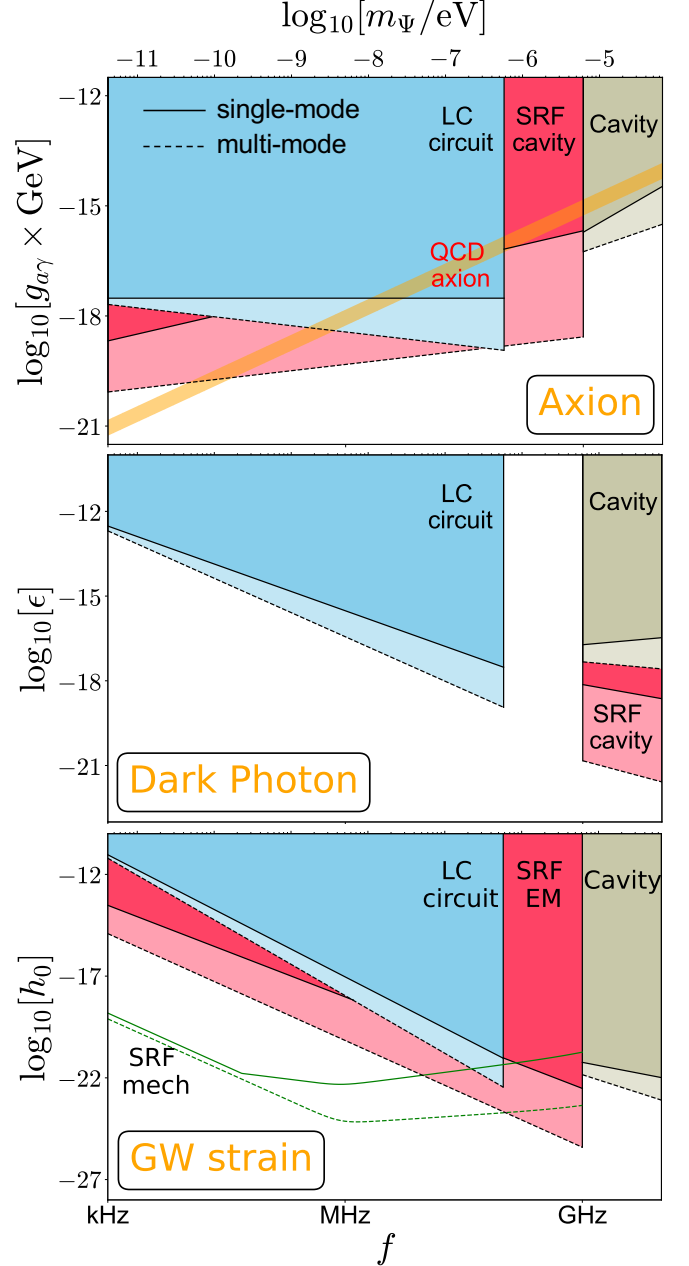


FIG. 1: Sensitivity reach of the axion and dark photon DM, and GW strain discussed are shown with solid and dashed lines representing the single-mode and multi-mode limit, respectively. The integration time spent in each e -fold of $\bar{\omega}_{\Psi}$ is $t_e = 10^7$ s. Benchmark parameters of different experimental setups are discussed in Supplemental Material II.

By considering only the intrinsic noise within $\Delta\omega_r$, SNR^2 for a given hypothesis of $\bar{\omega}_{\Psi}$ is simplified to

$$\text{SNR}^2(\bar{\omega}_{\Psi}) \simeq \frac{t_e}{\bar{\omega}_{\Psi}} \Delta\omega_{\Psi} \Delta\omega_r \frac{\alpha^4 S_{\Psi}^2}{32\pi\gamma^2 n_{\text{occ}}^2} \Big|_{\omega=\bar{\omega}_{\Psi}}. \quad (7)$$

From Eq. (7), the figure of merit is the response width

$\Delta\omega_r$ in Eq. (5), which is proportional to the scan rate in Ref. [34–37]. This parameter can be optimized by adjusting the readout coupling, specifically setting $\gamma_r = 2\gamma$ in the zero-temperature limit [40], or $\gamma_r \simeq 2n_{\text{occ}}\gamma$ for $n_{\text{occ}} \gg 1$ [38, 39, 41–43], rendering $\Delta\omega_r \simeq 3\gamma$ and $2n_{\text{occ}}\gamma$, respectively. Substituting these values back into Eq. (7) yields the sensitivity limit of single-mode resonators. The results are presented as solid lines in Fig. 1 for axion and dark photon DM with mass m_b , as well as GW strain h_0 at frequency f . The axion-photon coupling $g_{a\gamma}$ and kinetic mixing coefficient ϵ appear in α , while S_Ψ contains h_0^2 . Cavities or LC circuits with static magnetic fields [10, 11, 27, 28] require $\bar{\omega}_\Psi$ to be near ω_{rf} for each scan. On the other hand, superconducting radio-frequency (SRF) cavities using oscillating pump modes at $\omega_0 \simeq \omega_{\text{rf}}$ [32, 33, 41, 42, 47] allow $\bar{\omega}_\Psi$ of axion or GW to be much lower than ω_{rf} , enabling the upconversion of the pump mode. We illustrate both the electromagnetic coupling and the mechanical coupling for GW detection by SRF [33]. Details and benchmark parameters for each type of detector are in Supplemental Material II.

Quantum limit for multi-mode resonators — To surpass the quantum limit for single-mode resonators, one effective approach is to incorporate multiple auxiliary modes, such as a chain of detectors with the interaction Hamiltonian [49, 50]:

$$H_{\text{ch}} = \sum_{k=0}^{N-1} \left(i g \hat{a}_k \hat{a}_{k+1}^\dagger + i G \hat{a}_k \hat{a}_{k+1} + h.c. \right). \quad (8)$$

Here, the parameters g and G represent the couplings for beam-splitter-type and non-degenerate parametric interactions [51–55], respectively. The system comprises $N+1$ modes denoted by \hat{a}_k , with each adjacent pair linked by the two types of interactions. The dynamics described by Eq. (8) can be interpreted as two copies of the Hatano-Nelson model [56], where two groups of quadratures are amplified in opposite directions [50]. We designate \hat{a}_0 as the probing sensor, while the readout port is connected to the last mode \hat{a}_N , as illustrated in Fig. 2. The application of the $N = 1$ model of Eq. (8) for axion DM was discussed in [46, 57].

The chain model in Eq. (8) exhibits intrinsic noise PSDs contributions from all modes, represented as $\Sigma_k |S_{kr}|^2 n_{\text{occ}}$. To simplify the scattering matrix elements toward the readout port, we assume universal intrinsic dissipation $\gamma_k = \gamma$, resulting in

$$S_{kr} = \frac{-2\sqrt{\gamma}\gamma_r \mathcal{G}^{N-k} f_k}{\gamma_r f_N + f_{N+1}}, \quad S_{rr} = \frac{-\gamma_r f_N + f_{N+1}}{\gamma_r f_N + f_{N+1}}, \quad (9)$$

with a detailed derivation provided in Supplemental Material III. Here, $f_x \equiv \sum_{j=0}^{\lfloor x/2 \rfloor} C_{x-j}^j (\gamma - i\Omega)^{x-2j} \mathcal{J}^{2j}$, where $\lfloor \dots \rfloor$ denotes the integer value and C_{x-j}^j is the binomial coefficient. Additionally we introduce $\mathcal{J} \equiv (|g|^2 - |G|^2)^{1/2}$ and $\mathcal{G} \equiv |g| \pm |G|$, with the \pm sign distinguishing

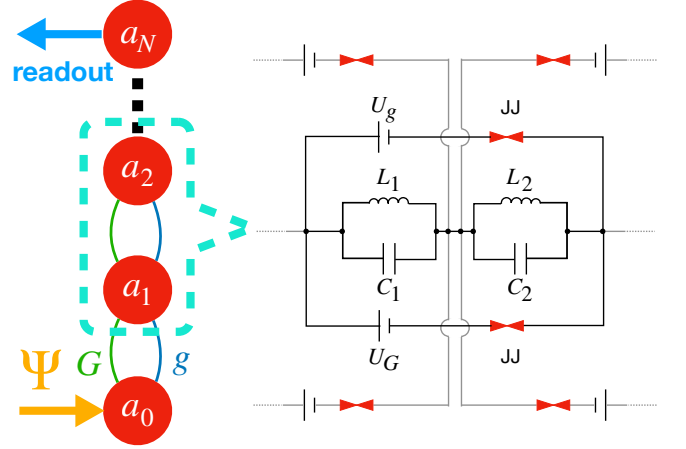


FIG. 2: Illustration of a chain of resonant modes described by Eq. (8). Each adjacent pair of modes is interconnected through both beam-splitter-type interactions (blue) and non-degenerate parametric interactions (green). The right panel demonstrates a straightforward implementation of these couplings using DC Josephson Junction effects.

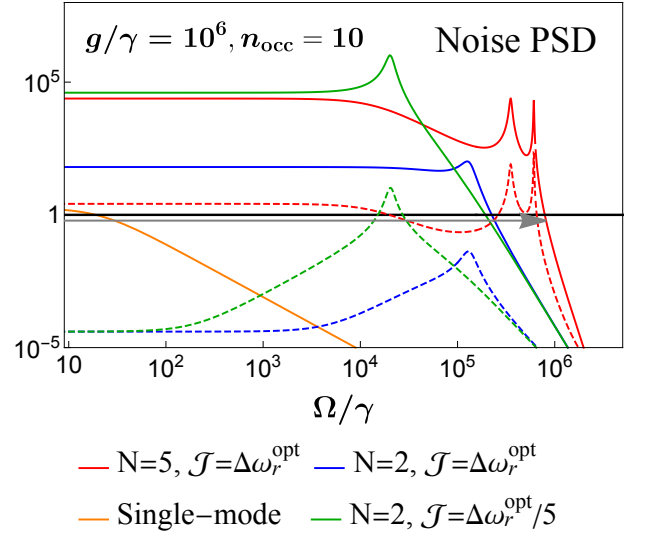


FIG. 3: Noise PSDs of the chain detectors assuming $g/\gamma = 10^6$, $n_{\text{occ}} = 10$, and $\gamma_r = \Delta\omega_r^{\text{opt}}$. The readout noise is represented by the black line, while the other solid lines depict the dominant contribution from \hat{a}_0 , which surpasses the remaining intrinsic noise illustrated by the dashed lines. A decrease in \mathcal{J} results in a squeezed spectrum. The gray arrow line indicates the range where Eq. (10) applies, specifically for $N = 5$. For comparison, the intrinsic noise of a single-mode resonator is also shown.

between different quadratures. For system stability, it is required that $|g| > |G|$ [49]. Notably, when $|g|$ significantly exceeds both γ and \mathcal{J} , sequential amplification

occurs for half quadratures when flowing from \hat{a}_0 to \hat{a}_N , while the other half decreases. In the following we will focus solely on the continuously amplified quadratures.

As previously mentioned, the sensitivity reach in Eq. (5) is governed by the response width. It can be either optimized numerically using Eq. (5), or approximated as the range in which intrinsic noise in \hat{a}_0 dominates over the other noise contributions. This approximation is given by the inequality:

$$|S_{0r}|^2 n_{\text{occ}} \gtrsim |S_{rr}|^2 \frac{1}{2} + \frac{1}{2} + \sum_{k=1}^N |S_{kr}|^2 n_{\text{occ}}. \quad (10)$$

To proceed, we initially examine the range that satisfies a necessary condition from Eq. (10): the dominance of the left-hand side over the readout noise on the right-hand side, characterized by a nearly constant PSD of approximately 1 for sufficiently small γ . By maintaining fixed values for g , γ , and n_{occ} , we then manipulate $\gamma_r = \mathcal{J}$. Intriguingly, in the left-hand domain, the condition $|S_{0r}|^2 \gg 1$ remains valid in the region where $\Omega \ll \gamma_r$, but it diminishes swiftly beyond this boundary. Leveraging this observation, we make replacements: \mathcal{J} , γ_r , and Ω are substituted with $\Delta\omega_r$, leading to an optimized response width:

$$\Delta\omega_r^{\text{opt}} \simeq \left(\gamma n_{\text{occ}} \mathcal{G}^{2N} \right)^{1/(2N+1)}, \quad (11)$$

which converges to $2|g|$ for large N . Fig. 3 depicts numerical instances of noise PSDs, with $\gamma_r = \Delta\omega_r^{\text{opt}}$ held constant and \mathcal{J} varied. In these scenarios, the remaining condition from Eq. (10), dictating that intrinsic noise in \hat{a}_0 surpasses other intrinsic noise sources, is inherently fulfilled. The figure underscores that a smaller value of \mathcal{J} mildly affects $\Delta\omega_r$, despite compressing the PSD within a narrower Ω range. By opting for $\gamma_r = \mathcal{J} = \Delta\omega_r^{\text{opt}}$, we achieve a consistently flat PSD within $\Delta\omega_r$, thereby rendering it robust against potential \mathcal{J} variations, in light of the reasonable demands for dynamic range.

It is noteworthy that both quadratures can be successively amplified by introducing additional auxiliary modes [44, 45]. The binary tree scenario, as introduced in [45] and Supplemental Material III, exhibits the same scaling of the response width as demonstrated in Eq. (11). Furthermore, this scenario allows for the incorporation of multiple probing sensors, leading to a further enhancement in the scan rate. In summary, by expanding the response width from order $n_{\text{occ}}\gamma$ to $|g|$, multi-mode resonators can significantly exceed the standard quantum limit of single-mode resonators, as illustrated in Fig. 3.

Simultaneous resonant and broadband detection — The sensitive response width depends on the two couplings in Eq. (8), making their experimental implementation crucial. One circuit diagram design, as illustrated in the right panel of Fig. 2, involves a parallel connection of each pair of adjacent modes using two

direct-current (DC) driven Josephson junctions [58]. The interaction Hamiltonian of the pair is

$$H_{\text{JJ}} = - \sum_{c=g,G} E_J^c \cos[\omega_d^c t + 2e_0(\Phi_k + \Phi_{k+1}) + \varphi_0^c], \quad (12)$$

where E_J^c represents the Josephson coupling energy, $\omega_d^c \equiv 2e_0 U^c$ is the driven frequency from DC voltage U^c , Φ_k denotes the phase coordinates of each mode, and φ_0^c is used to calibrate all g and G to the same phase. By setting $\omega_d^{g/G} = |\omega_{\text{rf}}^k \mp \omega_{\text{rf}}^{k+1}|$ in Eq. (12) and applying the rotating wave approximation (RWA), one can realize Eq. (8) with

$$|g| = 2e_0^2 \kappa_k \kappa_{k+1} E_J^g, \quad |G| = 2e_0^2 \kappa_k \kappa_{k+1} E_J^G, \quad (13)$$

respectively, where κ_k represents the zero-point uncertainties of Φ_k as discussed in Supplemental Material I. In order to avoid high-order expansions of $2\kappa_k(\hat{a}_k^\dagger \hat{a}_k)^{1/2}$ from Eq. (12), κ_k should be below $\mathcal{O}(1)$. Experimental achievement of Josephson coupling energies much higher than $\mathcal{O}(1)$ GHz has been demonstrated [59, 60]. Therefore, both g and G in Eq. (13) can be comparable to the resonant frequency of the signal modes considered in this study, resulting in the response width $\Delta\omega_r$ reaching the same order as ω_{rf} . However, a larger width poses challenges with the validity of the RWA when the frequency shift Ω is higher than or comparable to ω_{rf} , introducing terms other than those in Eq. (8) that can potentially terminate the sequential amplification. Other realizations of Eq. (8) can be found in [52–55].

The bandwidth $\Delta\omega_r$ covered by each scan is now capable of reaching the same order as ω_{rf} . For both axion and GW detection with static magnetic fields, as well as dark photon detection without background fields, it is imperative that $\bar{\omega}_\Psi$ falls within the vicinity of the bandwidth centered around ω_{rf} . Under such circumstances, Eq. (7) remains a viable approximation for determining the sensitivity reach, with the integration time t_{int} for each scan saturating t_e . Relative to single-mode resonators, multi-mode systems yield an increased sensitivity denoted by the ratio

$$\frac{\text{SNR}_{\text{MM}}^2}{\text{SNR}_{\text{SM}}^2} \simeq \frac{Q_{\text{int}}}{n_{\text{occ}}}, \quad (14)$$

where ‘MM’ and ‘SM’ correspond to multi-mode and single-mode, respectively. The multi-mode sensitivity reach is depicted by dashed lines in Fig. 1. Notably, Eq. (14) exhibits a significant enhancement for SRF detection of dark photon, assuming $Q_{\text{int}} = 10^{12}$ and $n_{\text{occ}} = 100$.

On the other hand, an operating pump mode with frequency ω_0 in an SRF enables excitation of the pump mode into a signal mode around $\omega_{\text{rf}} \simeq \omega_0 + \bar{\omega}_\Psi$, where $\bar{\omega}_\Psi$ can be significantly lower than ω_{rf} . Notably, when the multi-mode extension to SRF is employed, a wide range of $\bar{\omega}_\Psi$ spanning several orders of magnitude can

We are grateful to Raffaele Tito D’Agnolo, Nick Houston, Minyuan Jiang, Yonatan Kahn, Yiqiu Ma, Jan Schütte-Engel, Tao Shi, and Bin Xu for useful discussions. This work is supported by the National Key Research and Development Program of China under Grant No. 2020YFC2201501. Y.C. is supported by VILLUM FONDEN (grant no. 37766), by the Danish Research Foundation, and under the European Union’s H2020 ERC Advanced Grant “Black holes: gravitational engines of discovery” grant agreement no. Gravitast-101052587, and the Munich Institute for Astro-, Particle and BioPhysics (MIAPbP) which is funded by the Deutsche Forschungsgemeinschaft (DFG, German Research Foundation) under Germany’s Excellence Strategy – EXC-2094 – 390783311, and by FCT (Fundação para a Ciência e Tecnologia I.P, Portugal) under project No. 2022.01324.PTDC. J.S. is supported by Peking University under startup Grant No. 7101302974 and the National Natural Science Foundation of China under Grants No. 12025507, No.12150015; and is supported by the Key Research Program of Frontier Science of the Chinese Academy of Sciences (CAS) under Grants No. ZDBS-LY-7003 and CAS project for Young Scientists in Basic Research YSBR-006.

-
- [1] J. Preskill, M. B. Wise, and F. Wilczek, *Phys. Lett. B* **120**, 127 (1983).
- [2] L. Abbott and P. Sikivie, *Phys. Lett. B* **120**, 133 (1983).
- [3] M. Dine and W. Fischler, *Phys. Lett. B* **120**, 137 (1983).
- [4] A. E. Nelson and J. Scholtz, *Phys. Rev. D* **84**, 103501 (2011), arXiv:1105.2812 [hep-ph].
- [5] P. Svrcek and E. Witten, *JHEP* **06**, 051 (2006), arXiv:hep-th/0605206.
- [6] S. A. Abel, M. D. Goodsell, J. Jaeckel, V. V. Khoze, and A. Ringwald, *JHEP* **07**, 124 (2008), arXiv:0803.1449 [hep-ph].
- [7] A. Arvanitaki, S. Dimopoulos, S. Dubovsky, N. Kaloper, and J. March-Russell, *Phys. Rev. D* **81**, 123530 (2010), arXiv:0905.4720 [hep-th].
- [8] M. Goodsell, J. Jaeckel, J. Redondo, and A. Ringwald, *JHEP* **11**, 027 (2009), arXiv:0909.0515 [hep-ph].
- [9] R. Peccei and H. R. Quinn, *Phys. Rev. Lett.* **38**, 1440 (1977).
- [10] P. Sikivie, *Phys. Rev. Lett.* **51**, 1415 (1983), [Erratum: *Phys.Rev.Lett.* 52, 695 (1984)].
- [11] P. Sikivie, *Phys. Rev. D* **32**, 2988 (1985), [Erratum: *Phys.Rev.D* 36, 974 (1987)].
- [12] P. Sikivie, N. Sullivan, and D. Tanner, *Phys. Rev. Lett.* **112**, 131301 (2014), arXiv:1310.8545 [hep-ph].
- [13] S. Chaudhuri, P. W. Graham, K. Irwin, J. Mardon, S. Rajendran, and Y. Zhao, *Phys. Rev. D* **92**, 075012 (2015), arXiv:1411.7382 [hep-ph].
- [14] Y. Kahn, B. R. Safdi, and J. Thaler, *Phys. Rev. Lett.* **117**, 141801 (2016), arXiv:1602.01086 [hep-ph].
- [15] L. H. Nguyen, A. Lobanov, and D. Horns, *JCAP* **10**, 014 (2019), arXiv:1907.12449 [hep-ex].
- [16] A. V. Dixit, S. Chakram, K. He, A. Agrawal, R. K. Naik, D. I. Schuster, and A. Chou, *Phys. Rev. Lett.* **126**, 141302 (2021), arXiv:2008.12231 [hep-ex].
- [17] S. Ghosh, E. P. Ruddy, M. J. Jewell, A. F. Leder, and R. H. Maruyama, *Phys. Rev. D* **104**, 092016 (2021), arXiv:2104.09334 [hep-ph].
- [18] A. Caputo, A. J. Millar, C. A. J. O’Hare, and E. Vitagliano, *Phys. Rev. D* **104**, 095029 (2021), arXiv:2105.04565 [hep-ph].
- [19] R. Cervantes *et al.*, *Phys. Rev. D* **106**, 102002 (2022), arXiv:2204.09475 [hep-ex].
- [20] R. Cervantes, C. Braggio, B. Giaccone, D. Frolov, A. Grassellino, R. Harnik, O. Melnychuk, R. Pilipenko, S. Posen, and A. Romanenko, (2022), arXiv:2208.03183 [hep-ex].
- [21] Z. Tang *et al.*, (2023), arXiv:2305.09711 [hep-ex].
- [22] N. Aggarwal *et al.*, *Living Rev. Rel.* **24**, 4 (2021), arXiv:2011.12414 [gr-qc].
- [23] M. Gertsenshtein, *Sov.Phys.JETP* **41**, 84 (1962).
- [24] F. Pegoraro, E. Picasso, and L. A. Radicati, *J. Phys. A* **11**, 1949 (1978).
- [25] F. Pegoraro, L. A. Radicati, P. Bernard, and E. Picasso, *Phys. Lett. A* **68**, 165 (1978).
- [26] C. E. Reece, P. J. Reiner, and A. C. Melissinos, *Phys. Lett. A* **104**, 341 (1984).
- [27] N. Herman, A. Füzfa, L. Lehoucq, and S. Clesse, *Phys. Rev. D* **104**, 023524 (2021), arXiv:2012.12189 [gr-qc].
- [28] A. Berlin, D. Blas, R. Tito D’Agnolo, S. A. R. Ellis, R. Harnik, Y. Kahn, and J. Schütte-Engel, *Phys. Rev. D* **105**, 116011 (2022), arXiv:2112.11465 [hep-ph].
- [29] V. Domcke, C. Garcia-Cely, and N. L. Rodd, *Phys. Rev. Lett.* **129**, 041101 (2022), arXiv:2202.00695 [hep-ph].
- [30] A. V. Sokolov, (2022), arXiv:2203.03278 [hep-ph].
- [31] A. Berlin *et al.*, in *2022 Snowmass Summer Study* (2022) arXiv:2203.12714 [hep-ph].
- [32] M. E. Tobar, C. A. Thomson, W. M. Campbell, A. Quiskamp, J. F. Bourhill, B. T. McAllister, E. N. Ivanov, and M. Goryachev, *Symmetry* **14**, 2165 (2022), arXiv:2209.03004 [physics.ins-det].
- [33] A. Berlin, D. Blas, R. Tito D’Agnolo, S. A. R. Ellis, R. Harnik, Y. Kahn, J. Schütte-Engel, and M. Wentzel, (2023), arXiv:2303.01518 [hep-ph].
- [34] H. Zheng, M. Silveri, R. Brierley, S. Girvin, and K. Lehnert, (2016), arXiv:1607.02529 [hep-ph].
- [35] M. Malnou, D. A. Palken, B. M. Brubaker, L. R. Vale, G. C. Hilton, and K. W. Lehnert, *Phys. Rev. X* **9**, 021023 (2019), [Erratum: *Phys.Rev.X* 10, 039902 (2020)], arXiv:1809.06470 [quant-ph].
- [36] K. M. Backes *et al.* (HAYSTAC), *Nature* **590**, 238 (2021), arXiv:2008.01853 [quant-ph].
- [37] K. W. Lehnert (2021) arXiv:2110.04912 [quant-ph].
- [38] S. Chaudhuri, K. Irwin, P. W. Graham, and J. Mardon, (2018), arXiv:1803.01627 [hep-ph].
- [39] S. Chaudhuri, K. D. Irwin, P. W. Graham, and J. Mardon, (2019), arXiv:1904.05806 [hep-ex].
- [40] L. Krauss, J. Moody, F. Wilczek, and D. E. Morris, *Phys. Rev. Lett.* **55**, 1797 (1985).
- [41] A. Berlin, R. T. D’Agnolo, S. A. Ellis, C. Nantista, J. Neilson, P. Schuster, S. Tantawi, N. Toro, and K. Zhou, *JHEP* **07**, 088 (2020), arXiv:1912.11048 [hep-ph].
- [42] R. Lasenby, *Phys. Rev. D* **102**, 015008 (2020), arXiv:1912.11056 [hep-ph].
- [43] R. Lasenby, *Phys. Rev. D* **103**, 075007 (2021),

- arXiv:1912.11467 [hep-ph].
- [44] X. Li, M. Goryachev, Y. Ma, M. E. Tobar, C. Zhao, R. X. Adhikari, and Y. Chen, (2020), arXiv:2012.00836 [quant-ph].
 - [45] Y. Chen, M. Jiang, Y. Ma, J. Shu, and Y. Yang, *Phys. Rev. Res.* **4**, 023015 (2022), arXiv:2103.12085 [hep-ph].
 - [46] K. Wurtz, B. M. Brubaker, Y. Jiang, E. P. Ruddy, D. A. Palken, and K. W. Lehnert, *PRX Quantum* **2**, 040350 (2021), arXiv:2107.04147 [quant-ph].
 - [47] A. Berlin, R. T. D’Agnolo, S. A. R. Ellis, and K. Zhou, *Phys. Rev. D* **104**, L111701 (2021), arXiv:2007.15656 [hep-ph].
 - [48] R. H. Dicke, *Rev. Sci. Instrum.* **17**, 268 (1946).
 - [49] A. McDonald, T. Pereg-Barnea, and A. A. Clerk, *Phys. Rev. X* **8**, 041031 (2018), arXiv:1805.12557 [cond-mat.mes-hall].
 - [50] A. McDonald and A. A. Clerk, *Nature Commun.* **11**, 5382 (2020), arXiv:2004.00585 [quant-ph].
 - [51] J. Russer and P. Russer (2011) pp. 1–4.
 - [52] N. Bergeal, R. Vijay, V. E. Manucharyan, I. Siddiqi, R. J. Schoelkopf, S. M. Girvin, and M. H. Devoret, *Nature Physics* **6**, 296 (2010), arXiv:0805.3452 [cond-mat].
 - [53] B. Abdo, A. Kamal, and M. Devoret, *Phys. Rev. B* **87**, 014508 (2013), arXiv:1208.3142 [cond-mat].
 - [54] B. J. Chapman, B. A. Moores, E. I. Rosenthal, J. Kerckhoff, and K. W. Lehnert, *Applied Physics Letters* **108**, 222602 (2016), arXiv:1603.02716 [quant-ph].
 - [55] N. E. Frattini, U. Vool, S. Shankar, A. Narla, K. M. Sliwa, and M. H. Devoret, *Applied Physics Letters* **110**, 222603 (2017), arXiv:1702.00869 [cond-mat].
 - [56] N. Hatano and D. R. Nelson, *Phys. Rev. Lett.* **77**, 570 (1996).
 - [57] Y. Jiang, E. P. Ruddy, K. O. Quinlan, M. Malnou, N. E. Frattini, and K. W. Lehnert, *PRX Quantum* **4**, 020302 (2023), arXiv:2211.10403 [quant-ph].
 - [58] B. Josephson, *Physics Letters* **1**, 251 (1962).
 - [59] P. Dubos, H. Courtois, B. Panmetier, F. K. Wilhelm, A. D. Zaikin, and G. Schön, *Phys. Rev. B* **63**, 064502 (2001).
 - [60] T. E. Golikova, F. Hübler, D. Beckmann, N. V. Klenov, S. V. Bakurskiy, M. Y. Kupriyanov, I. E. Batov, and V. V. Ryazanov, *JETP Letters* **96**, 668 (2013).
 - [61] H. Wang, M. P. Blencowe, A. D. Armour, and A. J. Rimberg, *Phys. Rev. B* **96**, 104503 (2017).
 - [62] A. J. Brady, C. Gao, R. Harnik, Z. Liu, Z. Zhang, and Q. Zhuang, *PRX Quantum* **3**, 030333 (2022), arXiv:2203.05375 [quant-ph].
 - [63] J. W. Foster, Y. Kahn, R. Nguyen, N. L. Rodd, and B. R. Safdi, *Phys. Rev. D* **103**, 076018 (2021), arXiv:2009.14201 [hep-ph].
 - [64] Y. Chen, M. Jiang, J. Shu, X. Xue, and Y. Zeng, *Phys. Rev. Res.* **4**, 033080 (2022), arXiv:2111.06732 [hep-ph].
 - [65] D. A. Hill, *Electromagnetic fields in cavities: deterministic and statistical theories* (John Wiley & Sons, 2009).
 - [66] J. W. Foster, N. L. Rodd, and B. R. Safdi, *Phys. Rev. D* **97**, 123006 (2018), arXiv:1711.10489 [astro-ph.CO].

Supplemental Materials: Simultaneous Resonant and Broadband Detection for Dark Sectors

I: RESONANT ELECTROMAGNETIC SYSTEMS

In this section, we address the two electromagnetic resonant systems mentioned in the primary text: a resonant cavity and an LC circuit. We establish a parameterization for the interaction between quantized resonant modes and potential signals, such as an effective current. The left panel of Fig. S1 illustrates the two detection schemes. A cavity mode is generated resonantly once its frequency falls within the resonant bandwidth and its wave function spatially overlaps. Superconducting LC circuits employ pick-up loops to convert the magnetic flux induced by the effective current in a shielded room into a voltage signal. Furthermore, the appendix presents equivalent circuit representations of a cavity mode.

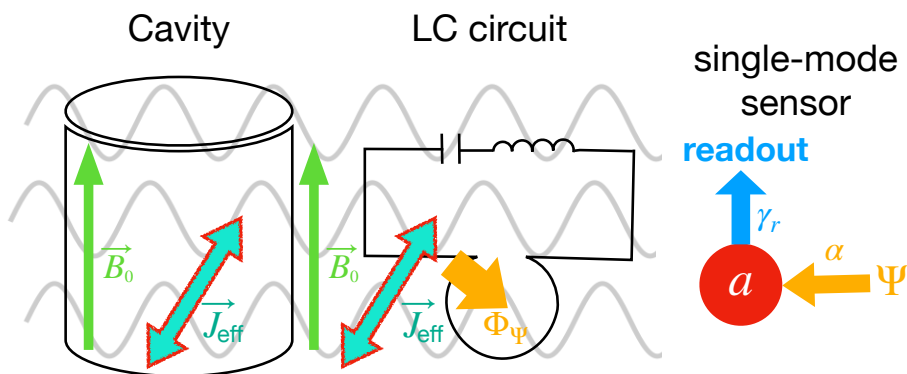


FIG. S1: The left panel depicts schematic plots illustrating the process by which a resonant cavity or a superconducting LC circuit captures the effective currents \vec{J}_{eff} originating from bosonic fields. Background magnetic fields \vec{B}_0 are utilized for the axion or GW detection. The right panel presents both scenarios using a depiction of a single-mode resonant sensor, which probes the dark sector labeled as Ψ and subsequently transmits the signal to the readout port.

Resonant cavity

One can compute the electromagnetic fields generated in the presence of an effective current denoted as J_{eff}^μ . To amplify this weak signal effectively, a resonant cavity with low dissipation, characterized by a significant quality factor Q_{int} , serves as a simple means. Within a cavity of volume V , the electromagnetic fields become quantized bound states, with their wavefunctions in the Coulomb gauge parameterized as follows:

$$\vec{A} = \sum_n \frac{1}{\sqrt{2\omega_{\text{rf}}^n}} \hat{a}_n^\dagger \vec{\epsilon}_n(\vec{r}) e^{-i\omega_{\text{rf}}^n t} + h.c.. \quad (\text{S1})$$

In the above equation, the discrete sum is taken over various modes labeled by n , and \hat{a}_n and \hat{a}_n^\dagger are annihilation and creation operators for a mode characterized by an eigenfrequency ω_{rf}^n and a wavefunction $\vec{\epsilon}_n(\vec{r})$. When considering a perfect conductor as the boundary, each mode arises from the solution to the vacuum Maxwell equations $\square \vec{A} = 0$, subject to the boundary conditions:

$$\hat{s} \times \vec{\epsilon}_n|_s = 0, \quad \hat{s} \cdot (\vec{\nabla} \times \vec{\epsilon}_n)|_s = 0. \quad (\text{S2})$$

Here, the subscript s denotes the surface of a cavity with a normal vector \hat{s} . Furthermore, the wavefunctions must satisfy the orthonormality condition:

$$\int \vec{\epsilon}_m^* \vec{\epsilon}_n d^3\vec{r} = \delta_{mn}. \quad (\text{S3})$$

Using Eq. S1, the free Hamiltonian for modes within the cavity can be written as:

$$H_0 = \frac{1}{2} \int_V (\vec{E}^2 + \vec{B}^2) d^3\vec{r} = \sum_n \omega_{\text{rf}}^n \left(\hat{a}_n^\dagger \hat{a}_n + \frac{1}{2} \right). \quad (\text{S4})$$

where $\vec{E} = -\partial\vec{A}/\partial t$ and $\vec{B} = \vec{\nabla} \times \vec{A}$ represent the electric and magnetic fields of the cavity modes, respectively.

We proceed by examining the interaction Hamiltonian concerning the spatial component of the effective current \vec{J}_{eff} . A linear coupling with the vector potential \vec{A} is readily established as follows:

$$H_{\text{int}} = \int_V \vec{A} \cdot \vec{J}_{\text{eff}} d^3\vec{r} = \sum_n \sqrt{\frac{V}{2\omega_{\text{rf}}^n}} \eta_n \bar{J}_{\text{eff}} \hat{a}_n^\dagger e^{-i\omega_{\text{rf}}^n t} + h.c.. \quad (\text{S5})$$

Here, η_n represents the geometric overlap function between $\vec{\epsilon}_n$ and \vec{J}_{eff} , defined as:

$$\eta_n \equiv \frac{\int_V \vec{\epsilon}_n \cdot \vec{J}_{\text{eff}} d^3\vec{r}}{\sqrt{\int_V |\vec{J}_{\text{eff}}|^2 d^3\vec{r}}}. \quad (\text{S6})$$

Moreover, \bar{J}_{eff} denotes the average current density within the cavity:

$$\bar{J}_{\text{eff}} \equiv \sqrt{\frac{1}{V} \int_V |\vec{J}_{\text{eff}}|^2 d^3\vec{r}}. \quad (\text{S7})$$

On the other hand, the time component of J_{eff}^μ , corresponding to the effective charge density ρ_{eff} , exclusively excites the irrotational mode [65], which does not experience resonant enhancement within the cavity context.

In conjunction with electromagnetic interaction involving the effective current, a cavity mode has the potential to be stimulated by an external force when a background cavity mode is existent. The force induces a displacement of the cavity wall, thereby instigating a power transition between the aforementioned modes. This phenomenon can be equivalently characterized by a linear coupling resembling the expression in Eq. (S5), which is demonstrated in the subsequent section.

LC circuit

The resonant frequency of a cavity is intrinsically linked to its spatial dimensions, posing a challenge in achieving a wide frequency tuning range beyond the GHz regime. However, this limitation can be mitigated through the utilization of an LC circuit, enabling precise tuning of the resonant frequency across different orders of magnitude below the GHz range. Comprising an inductor L and a capacitor C , this circuit forms a resonant system characterized by the resonant frequency $\omega_{\text{rf}} = 1/\sqrt{LC}$. The system's free Hamiltonian encompasses the energy stored within the inductor and the capacitor, represented as follows:

$$H_0 = \frac{\Phi^2}{2L} + \frac{Q^2}{2C} = \omega_{\text{rf}} \left(\hat{a}^\dagger \hat{a} + \frac{1}{2} \right). \quad (\text{S8})$$

Here, Φ denotes the magnetic flux traversing the inductor, and Q signifies the charge accumulated in the capacitor. The aforementioned equations are expanded utilizing annihilation and creation operators, with Φ and Q serving as the canonical coordinate and its conjugate momentum, respectively.

Introducing a pick-up loop, the LC circuit becomes capable of capturing an external magnetic flux Φ_Ψ and resonantly responding when the frequency of Φ_Ψ closely aligns with ω_{rf} . The interaction Hamiltonian, which arises from a shift of the canonical coordinate $\Phi \rightarrow \Phi + \Phi_\Psi$ within Eq. (S8), is presented as follows:

$$H_{\text{int}} = \frac{\Phi \Phi_\Psi}{L} = \sqrt{\frac{\omega_{\text{rf}}}{2L}} \Phi_\Psi \hat{a}_n^\dagger e^{-i\omega_{\text{rf}} t} + h.c.. \quad (\text{S9})$$

The magnetic flux present in the pick-up loop originates solely from the spatial component of the effective current. Within a shielded environment, this flux induces a magnetic field expressed as:

$$\vec{B}_\Psi(\vec{r}) \approx \int \frac{\vec{J}_{\text{eff}}(\vec{r}') \times (\vec{r} - \vec{r}')}{4\pi |\vec{r} - \vec{r}'|^3} d^3\vec{r}', \quad (\text{S10})$$

where we approximate it in the limit that the Compton wavelength of the source is much larger than the spatial scale of the detector.

Circuit representation of cavity modes

By encapsulating an antenna within a cavity, it becomes feasible to investigate specific cavity modes by analyzing the nodal flow across the antenna, which can be expressed as:

$$\Phi = \int_{\text{Ant}} \vec{A}(\vec{r}, t) \cdot d\vec{l} = \sum_n \kappa_n \hat{a}_n^\dagger e^{-i\omega_{\text{rf}}^n t} + h.c.. \quad (\text{S11})$$

Here, the integration spans the spatial extent of the antenna, and the zero-point uncertainty associated with a specific cavity mode is defined as:

$$\kappa_n \equiv \frac{1}{\sqrt{2\omega_{\text{rf}}^n}} \int_{\text{Ant}} \vec{\epsilon}_n(\vec{r}) \cdot d\vec{l}. \quad (\text{S12})$$

Given the harmonic oscillator behavior of both the Hamiltonians in Eq. (S4) and Eq. (S8), it becomes feasible to model a cavity mode through employment of an LC circuit, wherein the nodal flux is defined as in Eq. (S11), and the angular frequency is denoted as $\omega_{\text{rf}}^n = 1/\sqrt{L_n C_n}$. This correspondence leads to the following relationships:

$$L_n = \frac{2\kappa_n^2}{\omega_{\text{rf}}^n}, \quad C_n = \frac{1}{2\kappa_n^2 \omega_{\text{rf}}^n}. \quad (\text{S13})$$

II: SENSITIVITY REACH

This section evaluates sensitivity across detection setups by examining the interaction between resonant detectors and bosonic sources—axions, dark photons, and gravitational wave (GW) strain. These sources generate effective currents that can excite resonant modes in cavities or LC circuits (see Supplementary Material I). Additionally, GW strain can mechanically deform cavities, facilitating the transition from pump mode to signal mode.

Effective currents

As indicated earlier in the main discourse, the interaction Lagrangian between bosons and the electromagnetic field can be rearranged into the configuration $A_\mu J_{\text{eff}}^\mu$ to identify the effective currents J_{eff}^μ . The initial instance pertains to the axion-photon interaction, which can be expressed as follows:

$$\frac{1}{4} g_{a\gamma} a F_{\mu\nu} \tilde{F}^{\mu\nu} \rightarrow J_{\text{eff}}^{a\mu} = g_{a\gamma} \tilde{F}^{\mu\nu} \partial_\nu a. \quad (\text{S14})$$

Here, $g_{a\gamma}$ signifies the axion-photon coupling, a represents the axion field, while $F_{\mu\nu}$ and $\tilde{F}^{\mu\nu}$ denote the field strength tensor and the dual tensor of A_μ respectively. The Bianchi identity ensures that the derivative in Eq. (S14) exclusively affects the axion field. For scenarios involving non-relativistic axion dark matter, the term containing the time derivative effectively contributes to the axion's mass ($\omega_a \simeq m_a$), a value approximately 10^6 times greater than the momentum stemming from the spatial derivative [66]. As a result, a background magnetic field \vec{B}_0 is typically introduced for electromagnetic resonant detection, leading to the spatial current:

$$\vec{J}_{\text{eff}}^a = g_{a\gamma} \omega_a a \vec{B}_0. \quad (\text{S15})$$

Here \vec{B}_0 can exist in either a static or oscillating state.

The subsequent example pertains to the interaction involving the kinetic mixing dark photon A'^μ . This interaction can be captured by the coupling term in the interaction basis:

$$\epsilon m_{A'}^2 A'^\mu A_\mu \rightarrow J_{\text{eff}}^{A'\mu} = \epsilon m_{A'}^2 A'^\mu, \quad (\text{S16})$$

Here, ϵ signifies the kinetic mixing coefficient, while $m_{A'}$ represents the dark photon's mass. Unlike the axion case, the effective current in Eq. (S16) is solely dependent on the dark photon field, and thus, an electromagnetic background field is not relevant. Specifically, the spatial component of the current is directly proportional to \vec{A}' .

Finally, consideration is given to the GW strain, denoted as $h^{\mu\nu}$, featuring a universal coupling to matter fields. Its interaction with electromagnetic fields yields

$$\frac{1}{2}h^{\mu\nu}T_{\mu\nu}^{\text{EM}} \rightarrow J_{\text{eff}}^{h\mu} = \partial_\nu \left(\frac{1}{2}hF^{\mu\nu} + h^\nu{}_\rho F^{\rho\mu} - h^\mu{}_\rho F^{\rho\nu} \right). \quad (\text{S17})$$

Here, $T_{\mu\nu}^{\text{EM}}$ corresponds to the energy-momentum tensor of the electromagnetic field, and $h \equiv h^\rho{}_\rho$. Similar to the axion scenario, the generation of the effective current in Eq. (S17) requires a background electromagnetic field, established within the proper detector frame. Notably, while the GW strain is often computed in the transverse-traceless (TT) frame denoted by the amplitude h_0 , transitioning from the proper detector frame to h_0 introduces a scaling factor of $\omega_h^2 V^{2/3}$ [28, 29].

In scenarios characterized by a stationary magnetic field backdrop, the derivative in Eq. (S17) pertains exclusively to the GW strain [28], resulting in

$$\vec{J}_{\text{eff}}^h \simeq \omega_h^2 V^{1/3} B_0 h_0 \hat{j}(\vec{r}). \quad (\text{S18})$$

Here the spatially-dependent dimensionless vector $\hat{j}(\vec{r})$ is related to the incoming direction and polarization of the GW. In the context of heterodyne upconversion detection, ω_{rf} typically significantly outweighs ω_h , consequently rendering the dominant component in Eq. (S17) proportional to $\omega_{\text{rf}} \simeq V^{-1/3}$, thus leading to the same expression as in Eq. (S18).

As elaborated in Supplementary Material I, the spatial component of the effective currents exhibits coupling with either a cavity mode or a circuit mode through the following Hamiltonian expression:

$$H_\alpha = \alpha \Psi (\hat{a} e^{i\omega_{\text{rf}}t} + \hat{a}^\dagger e^{-i\omega_{\text{rf}}t}) / \sqrt{2}. \quad (\text{S19})$$

Here, the coupling coefficients α for the cavity and circuit scenarios are

$$\alpha_{\text{cav}} \Psi = \sqrt{\frac{V}{\omega_{\text{rf}}}} \eta \vec{J}_{\text{eff}}, \quad \alpha_{\text{LC}} \Psi = \sqrt{\frac{\omega_{\text{rf}}}{L}} \Phi_\Psi, \quad (\text{S20})$$

respectively, and are derived in accordance with Eq. (S5) and (S9).

The average current density, represented as \vec{J}_{eff} , can be directly inferred from Eq. (S15), (S16) and (S18) for respective source. The magnetic field strength B_0 is defined as the average magnitude within the relevant volume. The magnetic flux, Φ_Ψ , that traverses the pick-up loop of an LC circuit is intimately connected to the mean effective current density \vec{J}_{eff} by two factors: a spatial scale V and a dimensionless geometric parameter η , resulting in $\Phi_\Psi \sim \eta V \vec{J}_{\text{eff}}$. In this context, the inductance (L) is assumed as $V^{1/3}$ for the sake of simplicity. It is noteworthy that achieving an optimistic scaling for GW strain detection utilizing an LC circuit necessitates a specialized design of the pick-up loops, as introduced in Ref. [29]. The values of parameter α for each source and detection scheme are detailed in Table I.

Source \ Haloscope	Axion	Dark Photon	GW strain
LC circuit	$g_{a\gamma} \eta B_0 V^{5/6} \omega_a \sqrt{\omega_{\text{rf}}}$	$\epsilon \eta V^{5/6} m_{A'}^2 \sqrt{\omega_{\text{rf}}}$	$\eta B_0 V^{7/6} \omega_h^2 \sqrt{\omega_{\text{rf}}}$
Cavity	$g_{a\gamma} \eta B_0 V^{1/2} \omega_a / \sqrt{\omega_{\text{rf}}}$	$\epsilon \eta V^{1/2} m_{A'}^2 / \sqrt{\omega_{\text{rf}}}$	$\eta B_0 V^{5/6} \omega_h^2 / \sqrt{\omega_{\text{rf}}}$
SRF EM	$g_{a\gamma} \eta B_0 V^{1/2} \omega_a / \sqrt{2\omega_{\text{rf}}}$	$\epsilon \eta V^{1/2} m_{A'}^2 / \sqrt{\omega_{\text{rf}}}$	$\eta B_0 V^{7/6} \omega_h^2 \sqrt{\omega_{\text{rf}}/2}$
SRF Mechanical	/	/	$\eta_p^t \eta_p^h L_p(\omega_h) B_0 V^{1/2} \omega_h^2 \sqrt{\omega_{\text{rf}}/2}$

TABLE I: Effective couplings α between bosons and sensor modes in Eq. (S19) are listed.

Mechanical deformation

In addition to the direct coupling between GW and electromagnetic fields, an alternative mechanism for inducing cavity mode transitions involves the deformation of the cavity inner surface driven by GW, as explored in Ref. [33] for the SRF cavity configuration. The deformation of the cavity shell is characterized by local displacement from its equilibrium position, represented as

$$\vec{U}(\vec{r}, t) = \sum_p u_p(t) \vec{U}_p(\vec{r}), \quad (\text{S21})$$

where the subscript p corresponds to a mechanical normal mode. Here, \vec{r} denotes a point situated within the cavity shell with a volume of V_S , and $\vec{U}_p(\vec{r})$ describes the dimensionless spatial profile of the p -mode, satisfying the normalization condition

$$\int_{V_S} \vec{U}_p^*(\vec{r}) \cdot \vec{U}_q(\vec{r}) \rho_S(\vec{r}) d^3\vec{r} = \delta_{pq} M_S, \quad (\text{S22})$$

where $\rho_S(\vec{r})$ and M_S denote the mass density and total mass of the cavity shell, respectively. These mechanical normal modes can be excited in the presence of an external force, described by the following equation of motion:

$$\ddot{u}_p + \frac{\omega_p}{Q_p} \dot{u}_p + \omega_p^2 u_p = \frac{1}{M_S} \int_{V_S} \vec{f}(\vec{r}, t) \cdot \vec{U}_p^*(\vec{r}) d^3\vec{r} \equiv \frac{F_p}{M_S}. \quad (\text{S23})$$

Here ω_P and Q_P represent the resonant frequency and mechanical quality factor of the p -mode, respectively. The force density is denoted as $\vec{f}(\vec{r}, t)$, and F_p stands for the total force applied to the p -mode. The solution to this equation in the frequency domain is straightforwardly obtained as $u_p(\omega) = L_p(\omega) F_p(\omega) / M_S$, with $L_p(\omega)$ as the response function given by $(\omega^2 - \omega_p^2 + i\omega\omega_p/Q_p)^{-1}$.

GW strain acts as a tidal force on the cavity shell, exerting a force density $f_i = -\rho_S R_{i0j0} r^j$ in the long-wavelength regime, where r_j is defined in a coordinate system originating at the center of mass of the cavity. The Riemann curvature tensor is typically expressed in terms of the strain in the TT gauge, $R_{i0j0} = -\ddot{h}_{ij}^{\text{TT}}/2 + \mathcal{O}(h^2)$. The strain-induced force on the p -mode, labeled as F_p^h , is then characterized through an overlapping function η_p^h between the strain polarization basis H_{ij}^{TT} and the mechanical mode profile:

$$F_p^h(\omega) = M_S V^{1/3} \eta_p^h \omega^2 h_0(\omega), \quad \eta_p^h \equiv \frac{H_{ij}^{\text{TT}}}{2V^{1/3}M_S} \left| \int_{V_S} \rho(\vec{r}) U_p^{i*}(\vec{r}) r^j d^3\vec{r} \right|. \quad (\text{S24})$$

Here, $h_0(\omega)$ represents the strain amplitude, satisfying the relation $h_{ij}^{\text{TT}} \equiv h_0 H_{ij}^{\text{TT}}$.

The deformation of the inner cavity surface leads to deviations from the orthonormality condition of the cavity modes in Eq. (S3), enabling the transition from the pump mode to the signal mode. The effective coupling between these modes in the frequency domain is identified as per the following equation [33]:

$$\alpha\Psi(\omega) = \frac{\sqrt{2} \omega_{\text{rf}}^{1/2} B_0 V^{1/6}}{2 M_S} \sum_p \eta_p^t L_p(\omega - \omega_0) F_p^h(\omega - \omega_0). \quad (\text{S25})$$

Here, η_p^t represents the transition form factor given by

$$\eta_p^t = V^{1/3} \left| \int_S \left(\vec{\epsilon}_0 \cdot \vec{\epsilon}_1^* - \frac{1}{\omega_{\text{rf}}^2} (\nabla \times \vec{\epsilon}_0) \cdot (\nabla \times \vec{\epsilon}_1^*) \right) d\vec{s} \cdot \vec{U}_p \right|, \quad (\text{S26})$$

where the integral is performed over the inner surface of the cavity. The subscripts 0 and 1 denote the pump and signal modes, respectively. For simplicity, it is assumed that the dominant contribution from GW is manifested in a single quadrupolar mechanical mode possessing the lowest ω_p . This is attributed to the scaling relation $\eta_p^h \propto 1/\omega_p^2$. The value of the effective coupling is listed in Table. I as well.

On the other hand, thermal vibrations of the cavity shell can be represented as random forces F_p^T , leading the pump mode to transition into noise in the signal mode. According to the equipartition theorem, the PSD for F_p^T is given by $S_{F_p^T} = 4\pi M_S \omega_p T / Q_p$. Their contribution to the noise can be quantified through an additional occupation number as follows:

$$n_{\text{occ}}^{\text{mech}} = \frac{Q_{\text{int}} B_0^2 V^{1/3}}{4\pi M_S^2} \frac{\omega_0^5}{\omega^3 \omega_{\text{rf}}^2} \sum_p S_{F_p} |\eta_p^t L_p(\omega - \omega_0)|^2. \quad (\text{S27})$$

This contribution significantly outweighs the conventional thermal noise at low frequencies around kHz when $\eta_p^t \sim \mathcal{O}(1)$ [33].

Sensitivity reach

The sensitivity reach is contingent upon the power spectral densities (PSDs) of both the signal and the noise. These PSDs can be expressed as follows:

$$\begin{aligned} S_{\text{sig}} &= |S_{0r}|^2 \frac{\alpha^2}{4\gamma} S_{\Psi}, \\ S_{\text{noise}} &= \sum_{k=0}^N |S_{kr}|^2 n_{\text{occ}} + |S_{rr}|^2 \frac{1}{2} + \frac{1}{2}. \end{aligned} \quad (\text{S28})$$

Here, S_{kr} and S_{rr} denote the scattering matrix elements corresponding to the input (0) and readout (r) ports, respectively. The noise occupation number is denoted as n_{occ} , which arises from either thermal noise characterized by $n_{\text{occ}}^{\text{th}} = 1/2 + 1/(e^{\omega/T} - 1)$ or mechanical noise $n_{\text{occ}}^{\text{mech}}$ as defined in Eq. (S27). The intrinsic dissipation coefficient of the probing sensor is represented as $\gamma \equiv \omega/(2Q_{\text{int}})$. The PSD for a stochastic background source is given by

$$S_{\Psi} = \frac{2\pi}{\omega^2} \frac{d\rho_{\Psi}}{d\omega}, \quad (\text{S29})$$

where ρ_{Ψ} corresponds to the energy density of the boson background. For convenience, we introduce the concept of the average source frequency as

$$\bar{\omega}_{\Psi} \equiv \frac{\int \omega^2 S_{\Psi} \alpha^2 / \gamma d\omega}{\int \omega S_{\Psi} \alpha^2 / \gamma d\omega}, \quad (\text{S30})$$

and define the source bandwidth as

$$\Delta\omega_{\Psi} \equiv \frac{\int \omega^2 S_{\Psi} \alpha^2 / \gamma d\omega}{\bar{\omega}_{\Psi}^2 S_{\Psi}(\bar{\omega}_{\Psi}) \alpha^2(\bar{\omega}_{\Psi}) / \gamma(\bar{\omega}_{\Psi})}. \quad (\text{S31})$$

The quality factor of the source is defined as $Q_{\Psi} \equiv \bar{\omega}_{\Psi} / \Delta\omega_{\Psi}$, and it is assumed to be significantly larger than 1.

Now we have all the ingredients to delve into the sensitivity reach, which can be approximated by achieving a signal-to-noise ratio (SNR) of order one for a given hypothesis [38, 39, 41–43, 45]. For each scan, the SNR pertaining to a source with an average source frequency $\bar{\omega}_{\Psi}$ and a source bandwidth $\Delta\omega_{\Psi}$ is estimated as follows:

$$\text{SNR}^2 = \frac{t_{\text{int}}}{2\pi} \int \left(\frac{S_{\text{sig}}}{S_{\text{noise}}} \right)^2 d\omega \simeq \frac{t_{\text{int}} \Delta\omega_{\text{min}}}{2\pi} \frac{S_{\text{sig}}^2(\bar{\omega}_{\Psi})}{S_{\text{noise}}^2(\bar{\omega}_{\Psi})}. \quad (\text{S32})$$

Here, t_{int} represents the integration time allocated during the scan step, necessitating duration surpassing both the correlation time of the sources and the sensor systems' ring-up time.

where t_{int} is the integration time spent in the scan step, which is required to be longer than the correlation time of the sources and ring-up time of the sensor systems. $\Delta\omega_{\text{min}} = \min[\Delta\omega_{\Psi}, \Delta\omega_r]$ denotes the bandwidth of $(S_{\text{sig}}/S_{\text{noise}})^2$, where $\Delta\omega_r$ signifies the detector's response bandwidth, characterized by

$$\Delta\omega_r \equiv \int_{\omega_{\text{rf}}}^{\infty} \left(\frac{|S_{0r}|^2 n_{\text{occ}}}{S_{\text{noise}}} \right)^2 d\omega, \quad (\text{S33})$$

and signifies the frequency range dominated by intrinsic fluctuations over readout noise. Thus, the approximation

$$\frac{S_{\text{sig}}^2(\bar{\omega}_{\Psi})}{S_{\text{noise}}^2(\bar{\omega}_{\Psi})} \simeq \frac{\alpha^4 S_{\Psi}^2}{16\gamma^2 n_{\text{occ}}^2} \Big|_{\omega=\bar{\omega}_{\Psi}}, \quad (\text{S34})$$

can be employed in Eq. (S32). For the region where $\bar{\omega}_{\Psi} \geq \max[\Delta\omega_{\Psi}, \Delta\omega_r]$, the time distribution in each e -fold of $\bar{\omega}_{\Psi}$, denoted as t_e , can be described for each scan step by

$$t_{\text{int}} \simeq t_e \max[\Delta\omega_{\Psi}, \Delta\omega_r] / \bar{\omega}_{\Psi}. \quad (\text{S35})$$

Through the amalgamation of Eq. (S33), (S34) and (S35), Eq. (S32) can be reformulated as

$$\text{SNR}^2 = \frac{t_e}{\bar{\omega}_{\Psi}} \Delta\omega_{\Psi} \Delta\omega_r \frac{\alpha^4 S_{\Psi}^2}{32\pi\gamma^2 n_{\text{occ}}^2} \Big|_{\omega=\bar{\omega}_{\Psi}}. \quad (\text{S36})$$

The SNR for a GW strain can be estimated by substituting $S_\Psi(\bar{\omega}_\Psi)$ in Eq. (S36) with $h_0^2/\Delta\omega_h$.

We begin by examining a single-mode resonator characterized by two elements in its scattering matrix:

$$S_{0r} = -\frac{2\sqrt{\gamma\gamma_r}}{\gamma + \gamma_r - i\Omega}, \quad S_{rr} = \frac{\gamma - \gamma_r - i\Omega}{\gamma + \gamma_r - i\Omega}. \quad (\text{S37})$$

Here, γ_r denotes the readout coupling, while $\Omega \equiv \omega - \omega_{\text{rf}}$ represents the deviation in frequency from the resonant frequency. The optimization of $\Delta\omega_r$ can be achieved through the adjustment of γ_r , with the goal of maximizing the ranging satisfying $|S_{0r}|^2 n_{\text{occ}} \gtrsim |S_{rr}|^2 / 2 + 1/2$. The optimized value for γ_r leads to

$$\Delta\omega_r^{\text{opt}} \simeq 2 n_{\text{occ}} \gamma, \quad (\text{S38})$$

for scenarios with large n_{occ} , while for cases dominated by vacuum fluctuations, it is approximately $\Delta\omega_r^{\text{opt}} \simeq 3\gamma$. By incorporating Eq. (S38) and the couplings detailed in Table. I into Eq. (S36), the resulting SNR² can be obtained for each instance of single-mode resonant detection as well as for the sources in question:

- Axion:

$$\begin{aligned} \text{LC Circuit} &: (\pi/2) (g_{a\gamma}^4) \rho_{\text{DM}}^2 \eta^4 B_0^4 V^{10/3} Q_a Q_{\text{int}} t_e / T, \\ \text{Cavity} &: 3\pi (g_{a\gamma}^4 / m_a^5) \rho_{\text{DM}}^2 \eta^4 B_0^4 V^2 Q_a Q_{\text{int}} t_e, \\ \text{SRF} &: (\pi/8) (g_{a\gamma}^4 / m_a^2) \rho_{\text{DM}}^2 \eta^4 B_0^4 V^2 Q_a Q_{\text{int}} t_e / (\omega_{\text{rf}}^2 T). \end{aligned} \quad (\text{S39})$$

- Dark Photon:

$$\begin{aligned} \text{LC Circuit} &: (\pi/2) (\epsilon^4 m_{A'}^4) \rho_{\text{DM}}^2 \eta^4 V^{10/3} Q_{A'} Q_{\text{int}} t_e / T, \\ \text{Cavity} &: 3\pi (\epsilon^4 / m_{A'}^5) \rho_{\text{DM}}^2 \eta^4 V^2 Q_{A'} Q_{\text{int}} t_e, \\ \text{SRF} &: (\pi/2) (\epsilon^4 m_{A'}^2) \rho_{\text{DM}}^2 \eta^4 V^2 Q_{A'} Q_{\text{int}} t_e / (\omega_{\text{rf}}^2 T). \end{aligned} \quad (\text{S40})$$

- GW strain:

$$\begin{aligned} \text{LC Circuit} &: 1/(8\pi) (h_0^4 \omega_h^8) \eta^4 B_0^4 V^{14/3} Q_h Q_{\text{int}} t_e / T, \\ \text{Cavity} &: 3/(4\pi) (h_0^4 \omega_h^3) \eta^4 B_0^4 V^{10/3} Q_h Q_{\text{int}} t_e, \\ \text{SRF EM coupling} &: 1/(32\pi) (h_0^4 \omega_h^6) \eta^4 B_0^4 V^{14/3} Q_h Q_{\text{int}} t_e \omega_{\text{rf}}^2 / T. \\ \text{SRF mechanical coupling} &: 1/(16\pi) (h_0^4 \omega_h^6) |\eta_p^t \eta_p^h L_p(\omega_h)|^4 B_0^4 V^2 Q_h Q_{\text{int}} t_e \omega_{\text{rf}}^2 / (TN_M). \end{aligned} \quad (\text{S41})$$

In the context of SRF mechanical coupling, we introduce a dimensionless function $N_M(\omega_h)$ defined as follows:

$$N_M(\omega_h) \equiv 1 + Q_{\text{int}} \omega_{\text{rf}} B_0^2 S_{F_p} |\eta_p^t L_p(\omega_h)|^2 V^{1/3} / (\pi T M_S^2). \quad (\text{S42})$$

Here, the two constituent terms encapsulate the representations of thermal and mechanical noise, respectively. At frequencies below 100 kHz, the value of n_{occ} increases significantly, causing the optimized bandwidth in Eq. (S38) to exceed $\bar{\omega}_\Psi$. In this region, we set $t_{\text{int}} = t_e$.

Requiring each case mentioned above to achieve order one, we can establish the sensitivity reach for single-mode resonant detection, illustrated by the solid lines in Fig. 2 of the maintext. The e -fold time is designated as $t_e = 10^7$ s. The selected benchmark experimental parameters are as follows:

- LC circuit: $B_0 = 4$ T, $Q_{\text{int}} = 10^6$, $T = 0.01$ K, $V = 1$ m³;
- Cavity: $B_0 = 4$ T, $Q_{\text{int}} = 10^4$, $T = 0.01$ K, $V = 1$ m³;
- SRF: $B_0 = 0.2$ T, $Q_{\text{int}} = 10^{12}$, $T = 1.8$ K, $V = 1$ m³, $\omega_{\text{rf}} \simeq \omega_0 = 2\pi$ GHz.

For the cases involving axion and dark photon dark matter, we consider $Q_a = Q_{A'} = 10^6$ and $\rho_{\text{DM}} = 0.45$ GeV/cm³, while $Q_h = 10^3$ is assumed for GW strain. The overlapping factor η is set to 1 for the axion and $1/\sqrt{3}$ for the dark photon, considering the projections of the three polarization degrees of freedom. Notably, for the dark photon, the

SRF cavity is utilized similar to a traditional cavity without heterodyne upconversion, where ω_{rf} must match $m_{A'}$, probing only $m_{A'} \in (1 - 10)$ GHz is probed. For GW detection with electromagnetic coupling, $\eta = 1/10$ is adopted, in line with the order specified in Refs. [28, 29]. In contrast, for mechanical coupling, a distinct cavity shape is employed to maximize the deformation-induced transition. The associated parameters are $Q_p = 10^6$, $\omega_p = 10$ kHz, $M_S = 10$ kg, $\eta_p^t = 1$ and $\eta_p^h = 0.18$ [33].

In the context of a multi-mode resonator, as demonstrated in the main text, we establish that $\Delta\omega_r^{\text{opt}}$ can attain an order of magnitude comparable to the resonant frequency ω_{rf} . For a cavity with a static magnetic background and an LC circuit, this implies employing $\Delta\omega_r \approx \omega_{\text{rf}}$ in Eq. (S36), leading to the requirement that t_{int} matches t_e . Moreover, we set $\omega_{\text{rf}}/(2\pi) = 5$ GHz for the cavity detection, spanning the range from 1 to 10 GHz for a single scan. On the other hand, for the multi-mode extension involving SRF heterodyne upconversion with an oscillating electromagnetic field background, it becomes possible to encompass a response bandwidth spanning $\bar{\omega}_\Psi$ over several orders of magnitude. For instance, this coverage extends from $\omega_{\text{rf}} - \omega_0 = 2\pi$ kHz to $\omega_{\text{rf}} = 2\pi$ GHz, as elaborated upon in the maintext. In this scenario, the SNR^2 can be estimated by taking $t_{\text{int}} = 6 \ln 10 t_e$ in Eq. (S32). The SNR^2 values for multi-mode resonant detection are provided in the subsequent list:

- Axion:

$$\begin{aligned} \text{LC Circuit} &: (\pi/2) (g_{a\gamma}^4 m_a) \rho_{\text{DM}}^2 \eta^4 B_0^4 V^{10/3} Q_a Q_{\text{int}}^2 t_e / T^2, \\ \text{Cavity} &: 2\pi (g_{a\gamma}^4 / m_a^3) \rho_{\text{DM}}^2 \eta^4 B_0^4 V^2 Q_a Q_{\text{int}}^2 t_e / \omega_{\text{rf}}^2, \\ \text{SRF} &: (3\pi \ln 10 / 4) (g_{a\gamma}^4 / m_a) \rho_{\text{DM}}^2 \eta^4 B_0^4 V^2 Q_a Q_{\text{int}}^2 t_e / (\omega_{\text{rf}}^2 T^2). \end{aligned} \quad (\text{S43})$$

- Dark Photon:

$$\begin{aligned} \text{LC Circuit} &: (\pi/2) (\epsilon^4 m_{A'}^5) \rho_{\text{DM}}^2 \eta^4 V^{10/3} Q_{A'} Q_{\text{int}}^2 t_e / T^2, \\ \text{Cavity} &: 2\pi (\epsilon^4 m_{A'}) \rho_{\text{DM}}^2 \eta^4 V^2 Q_{A'} Q_{\text{int}}^2 t_e / \omega_{\text{rf}}^2, \\ \text{SRF} &: (\pi \ln 10 / 2) (\epsilon^4 m_{A'}^3) \rho_{\text{DM}}^2 \eta^4 V^2 Q_{A'} Q_{\text{int}}^2 t_e / (\omega_{\text{rf}}^2 T^2). \end{aligned} \quad (\text{S44})$$

- GW strain:

$$\begin{aligned} \text{LC Circuit} &: 1/(8\pi) (h_0^4 \omega_h^9) \eta^4 B_0^4 V^{14/3} Q_h Q_{\text{int}}^2 t_e / T^2, \\ \text{Cavity} &: 1/(2\pi) (h_0^4 \omega_h^5) \eta^4 B_0^4 V^{10/3} Q_h Q_{\text{int}}^2 t_e / \omega_{\text{rf}}^2, \\ \text{SRF EM coupling} &: 3 \ln 10 / (16\pi) (h_0^4 \omega_h^7) \eta^4 B_0^4 V^{14/3} Q_h Q_{\text{int}}^2 t_e \omega_{\text{rf}}^2 / T^2. \\ \text{SRF mechanical coupling} &: 3 \ln 10 / (16\pi) (h_0^4 \omega_h^7) |\eta_p^t \eta_p^h L_p(\omega_h)|^4 B_0^4 V^2 Q_h Q_{\text{int}}^2 t_e \omega_{\text{rf}}^2 / (TN_M)^2. \end{aligned} \quad (\text{S45})$$

III: INPUT-OUTPUT FORMALISM FOR SINGLE-MODE AND MULTI-MODE RESONATORS

In this section, we employ the input-output formalism to derive the scattering matrix elements for both single-mode and multi-mode resonators as discussed in the main text.

Single-mode resonator

The Hamiltonian governing a resonant mode \hat{a} is given by

$$H = H_0 + H_{\text{int}}, \quad (\text{S46})$$

where $H_0 = \omega_{\text{rf}}(\hat{a}^\dagger \hat{a} + 1/2)$ represents the free component, and H_{int} encompasses interaction terms. Employing the Heisenberg equation in the interaction picture,

$$\frac{d}{dt} \hat{a} = -i [\hat{a}, H_{\text{int}}], \quad (\text{S47})$$

facilitates the resolution of the system's dynamics.

Prior to delving into particular forms of interaction, we initially examine the environmental factors that manifest when the system is coupled to a external port, described by the quantum Langevin equation:

$$-i\left[\hat{a}, H_{\text{env}}^{\text{p}}\right] = -\gamma_{\text{p}}\hat{a} + \sqrt{2\gamma_{\text{p}}}\hat{u}_{\text{p}}, \quad (\text{S48})$$

where $H_{\text{env}}^{\text{p}}$ entails the interaction with the environment via port p, γ_{p} represents the dissipation coefficient, and \hat{u}_{p} corresponds to incoming noise according to the fluctuation-dissipation theorem. Additionally, the input-output relation

$$\hat{v}_{\text{p}} = \hat{u}_{\text{p}} - \sqrt{2\gamma_{\text{p}}}\hat{a}, \quad (\text{S49})$$

emerges from the port boundary condition, where \hat{v}_{p} designates the outgoing mode.

For a single-mode resonant detection system, two noise-contributing ports are of significance: intrinsic dissipation and readout. Together with the interaction with a potential signal, H_{α} introduced in Eq. (S19), the interaction Hamiltonian becomes

$$H_{\text{int}} = H_{\alpha} + H_{\text{env}}^{\gamma} + H_{\text{env}}^{\gamma_r}. \quad (\text{S50})$$

By utilizing Eq. (S47) and (S48), the equation of motion for \hat{a} in the frequency domain can be solved:

$$\hat{a} = \frac{-i\alpha\Psi e^{-i\omega_{\text{rf}}t}/\sqrt{2} + \sqrt{2\gamma}\hat{u}_a + \sqrt{2\gamma_r}\hat{u}_r}{\gamma + \gamma_r - i\Omega}, \quad (\text{S51})$$

where γ and γ_r denote the dissipation coefficients of the two ports with corresponding incoming modes \hat{u}_a and \hat{u}_r , respectively.

The observable obtained originates from the readout port's outgoing mode. As per the input-output relation in Eq. (S49), this is expressed as

$$\hat{v}_r = S_{0r} \left(\hat{u}_a - \frac{i\alpha e^{-i\omega_{\text{rf}}t}}{2\sqrt{\gamma}}\Psi \right) + S_{rr}\hat{u}_r, \quad (\text{S52})$$

where the two scattering matrix elements follow Eq. (S37), depicting the propagation of an incoming mode from one port to another.

When the integration time significantly exceeds the signal's correlation time, the PSD of the outgoing mode is utilized, defined by

$$S_{v_r}(\Omega)\delta(\Omega - \Omega') \equiv \langle \hat{v}_r(\Omega)\hat{v}_r^*(\Omega') \rangle, \quad (\text{S53})$$

incorporating PSDs of both the signal and noise. The intrinsic fluctuation PSD is $\langle \hat{u}_a\hat{u}_a^{\dagger} \rangle = n_{\text{occ}}$, while the readout PSD can be quantum-limited: $\langle \hat{u}_r\hat{u}_r^{\dagger} \rangle = 1/2$, resulting in

$$S_{v_r} = |S_{0r}|^2 \left(n_{\text{occ}} + \frac{\alpha^2}{4\gamma} S_{\Psi} \right) + |S_{rr}|^2 \frac{1}{2}. \quad (\text{S54})$$

Multi-mode resonator with a chain structure

We proceed by examining a chain of resonant modes, where each neighboring pair is connected through both beam-splitter-type interactions and non-degenerate parametric interactions. The system is described by the Hamiltonian:

$$\begin{aligned} H_{\text{ch}} &= \sum_{k=0}^{N-1} \left(i|g|e^{i\varphi_k^g}\hat{a}_k\hat{a}_{k+1}^{\dagger} + i|G|e^{i\varphi_k^G}\hat{a}_k\hat{a}_{k+1} + h.c. \right) \\ &= \sum_{k=0}^{N-1} \left[(|g| - |G|)X_k\tilde{Y}_{k+1} - (|g| + |G|)\tilde{X}_{k+1}Y_k \right], \end{aligned} \quad (\text{S55})$$

where $\varphi_k^{g/G}$ are the relative phases of the couplings. The quadrature operators are introduced:

$$\begin{aligned} X_k &\equiv \frac{e^{i\varphi_k^+}}{\sqrt{2}}\hat{a}_k + h.c., & Y_k &\equiv \frac{e^{i\varphi_k^+}}{\sqrt{2}i}\hat{a}_k + h.c., \\ \tilde{X}_k &\equiv \frac{e^{i\varphi_{k-1}^-}}{\sqrt{2}}\hat{a}_k + h.c., & \tilde{Y}_k &\equiv \frac{e^{i\varphi_{k-1}^-}}{\sqrt{2}i}\hat{a}_k + h.c.. \end{aligned} \quad (\text{S56})$$

Here $\varphi_k^\pm \equiv (\varphi_k^G \pm \varphi_k^g)/2$. As noted in the maintext, the probe sensor mode and the readout port are strategically positioned at the two opposing termini of the chain, specifically labeled as \hat{a}_0 and \hat{a}_N , respectively. We focus on the scattering matrix elements that characterize propagation across the chain.

Assuming the relative phases $\varphi_k^{g/G}$ are zero, resulting in $X_k = \tilde{X}_k$ and $Y_k = \tilde{Y}_k$, we obtain decoupled equations of motion for Y_k as:

$$\begin{aligned} (\gamma - i\Omega)Y_0 + (|g| - |G|)Y_1 &= \sqrt{2\gamma}\hat{u}_0, \\ (\gamma - i\Omega)Y_k + (|g| - |G|)Y_{k+1} - (|g| + |G|)Y_{k-1} &= \sqrt{2\gamma}\hat{u}_k, \\ (\gamma + \gamma_r - i\Omega)Y_N - (|g| + |G|)Y_{N-1} &= \sqrt{2\gamma}\hat{u}_N + \sqrt{2\gamma_r}\hat{u}_r, \end{aligned} \quad (\text{S57})$$

where $k = 1, 2, \dots, N-1$, and all the intrinsic dissipation coefficients are considered to be γ for the sake of simplicity. The recursive relations for Y_k are obtained from the first two lines in Eq. (S57):

$$Y_k = y_k \sum_{j=0}^k \prod_{m=j}^{k-1} \mathcal{G}^{k-j} y_m \sqrt{2\gamma}\hat{u}_j - \mathcal{G} y_k Y_{k+1}. \quad (\text{S58})$$

Here, we define the series y_k , \mathcal{J} , and \mathcal{G} as follows:

$$y_0 \equiv 1/(\gamma - i\Omega), \quad y_k \equiv 1/(\gamma - i\Omega + \mathcal{J}^2 y_{k-1}), \quad \mathcal{J} \equiv (|g|^2 - |G|^2)^{1/2}, \quad \mathcal{G} \equiv |g| + |G|. \quad (\text{S59})$$

The solution for Y_N is then expressed as:

$$Y_N = \frac{\sqrt{2\gamma_r}\hat{u}_r + \sum_{k=0}^N \prod_{j=k}^{N-1} \mathcal{G}^{N-k} y_j \sqrt{2\gamma}\hat{u}_k}{\gamma + \gamma_r - i\Omega + \mathcal{J}^2 y_{N-1}}. \quad (\text{S60})$$

The scattering matrix elements entering the readout port are given by:

$$S_{kr} = \frac{-2\sqrt{\gamma_r}\mathcal{G}^{N-k} f_k}{\gamma_r f_N + f_{N+1}}, \quad S_{rr} = \frac{-\gamma_r f_N + f_{N+1}}{\gamma_r f_N + f_{N+1}}, \quad (\text{S61})$$

where f_k is defined as:

$$f_k \equiv \prod_{j=0}^{k-1} \frac{1}{y_j} = \sum_{j=0}^{\lfloor k/2 \rfloor} C_{k-j}^j (\gamma - i\Omega)^{k-2j} \mathcal{J}^{2j}. \quad (\text{S62})$$

The stability condition $|g| > |G|$ [49] arises from the poles of the scattering matrix elements, under the assumption of negligible γ .

Similarly, we can solve the equations of motion for the variable X_k . These equations are distinguished from those governing Y_k solely by a change in the sign of the quantity $|G|$, denoted as $|G| \rightarrow -|G|$. In situations where the magnitude of $|g|$ significantly surpasses that of both γ and \mathcal{J} , the progression of Y_k or X_k results in consecutive increments or decrements, respectively.

On the other hand, when the relative phases $\varphi_k^{g/G}$ are present, the amplification of the k -th mode to the $(k+1)$ -th mode, denoted as Y_k , experiences a misalignment with the previously amplified \tilde{Y}_k . Instead, as defined in Eq. (S56), they are related by a linear transformation:

$$\tilde{X}_k = X_k \cos \theta_k - Y_k \sin \theta_k, \quad \tilde{Y}_k = X_k \sin \theta_k + Y_k \cos \theta_k. \quad (\text{S63})$$

Here, we define $\theta_k \equiv (\varphi_{k-1}^G - \varphi_{k-1}^g - \varphi_k^G - \varphi_k^g)/2$. Consequently, the amplification process experiences a sequence of attenuation factors expressed as the product $\prod_{k=1}^{N-1} \cos \theta_k$. It's important to observe that even with an initial calibration of all $\varphi_k^{g/G}$ fluctuations in the phase of the pumping modes have the potential to contribute to $\varphi_k^{g/G}$ [61].

Multi-mode resonator with a binary tree structure

Finally, we investigate a multi-mode resonator employing a binary tree configuration, as initially presented in Ref. [45]. The corresponding Hamiltonian, denoted as H_{BT} , is formulated as:

$$H_{\text{BT}} = \sum_{i=2}^N \sum_{j=1}^{2^{N-i}} i \hat{a}_{ij} \left(g \hat{a}_{i-1,2j-1}^\dagger + G \hat{c}_{i-1,2j-1} \right) + \sum_{i=2}^N \sum_{j=1}^{2^{N-i}} i \hat{c}_{ij} \left(g \hat{a}_{i-1,2j}^\dagger + G \hat{c}_{i-1,2j} \right) + i \hat{b} \left(g \hat{a}_{N1}^\dagger + G \hat{c}_{N1} \right) + h.c., \quad (\text{S64})$$

In this expression, the parameters g and G represent complex couplings. Similar to the chain-like structure introduced in Eq. (S55), the formulation in Eq. (S64) encompasses both beam-splitter-type interactions and non-degenerate parametric interactions. Moreover, it introduces auxiliary modes. An illustrative example of the model with $N = 3$ is presented in Fig. S2.

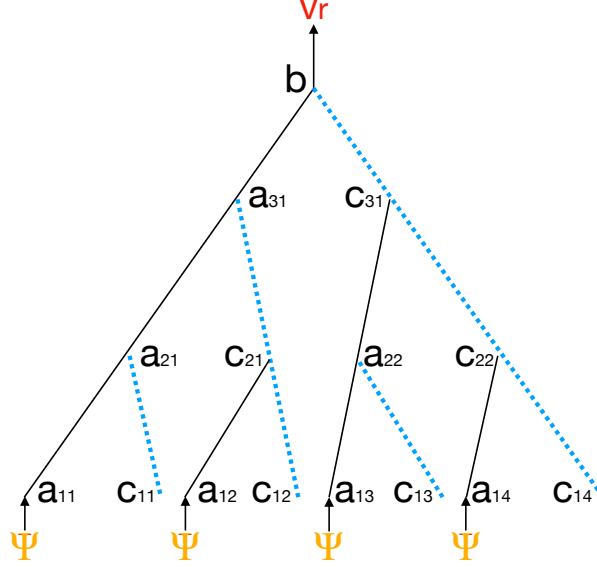


FIG. S2: An instance of a multi-mode resonator characterized by a binary tree structure with a specific instance having $N = 3$ is presented. Black lines delineate beam-splitter-like interactions, whereas blue dashed lines depict non-degenerate parametric interactions. At the lowest tier, a total of 2^N sensors are positioned, facilitating the probing of Ψ .

The equation of motion for a mode situated within the middle of the network can be expressed as:

$$\hat{c}_{ij} = \frac{\sqrt{2}\gamma \left[\hat{u}_{ij}^c - \left(g^* \hat{u}_{i-1,2j}^a + G^* \hat{u}_{i-1,2j}^{c\dagger} \right) / (\gamma - i\Omega) \right]}{\gamma - i\Omega + \mathcal{J}^2 / (\gamma - i\Omega)} + \dots, \quad (\text{S65})$$

where \dots accounts for terms involving modes not directly connected to \hat{c}_{ij} as well as the coupling with the higher-level mode. The equations of motion for \hat{a}_{ij} closely resemble Eq. (S65), with the sole distinction being the alteration of the subscript $2j$ to $2j - 1$. For $|g| \simeq |G| \gg \gamma$, the propagation from $\hat{u}_{i-1,2j}^a$ or $\hat{u}_{i-1,2j}^{c\dagger}$ to \hat{c}_{ij} in Eq. (S65) is amplified by a factor of $|g|/(\gamma - i\Omega)$. In this configuration, 2^N sensors are positioned at the bottom level to probe Ψ , each undergoing successive amplification as they propagate toward \hat{b} . Detailed numerical computations pertaining to optimized conditions and the corresponding sensitivity reach for axion are provided in Ref. [45].

Notably, unlike the chain model expressed in Eq. (S55), both quadratures of each mode within this binary tree structure are equally amplified. This quality mitigates the issues of phase fluctuations mentioned in the preceding subsection.